Research Article | Vol. 33, No. 25 / 15 Dec 2025 / Optics Express 52356
Optics EXPRESS

On-chip gain elements for integrated photonics

F. T. ALBELADI,[1,3] S. GILLGRASS,[2] P. MISHRA,[2] C. P. ALLFORD,[2] S. SHUTTS,[2] AND P. M. SMOWTON[2,4]

[1]Department of Physical Sciences, College of Science, University of Jeddah, Jeddah 21589, Saudi Arabia
[2]School of Physics and Astronomy, Cardiff University, The Parade, Cardiff. CF24 3AA, UK
[3]AlbeladiFT@Cardiff.ac.uk
[4]SmowtonPM@Cardiff.ac.uk

Abstract: The design of gain chips for hybrid integration with photonic integrated circuits (PICs) is studied and highlights the benefits of incorporating at least one reflector in the III-V gain material. Quantum dot (QD)-based gain chips with a multi-mode interference (MMI) reflector (MMIR) offer fabrication simplicity and good performance in the O-band. The inclusion of an MMIR in a ridge waveguide (RWG) laser reduces the threshold current by 87% (6 mA vs 46 mA for 1 mm length) and leads to higher slope efficiency, indicating over 90% mirror reflectivity, as compared to Fabry-Perot structures. Both 1- and 2-port designs will simplify alignment of active and passive waveguides for hybrid integration and are strong candidates for large-scale PIC applications.

1. Introduction

Innovations in photonic integrated circuits (PICs) are pivotal in many fields, including local area high-speed communication, quantum computing, and advanced sensing technologies. The increasing demand for compact, high-performance, and energy-efficient integrated laser sources for PICs has become a key area of research. Silicon photonics, which we here consider to make use of silicon on insulator (SOI) wafers and CMOS compatible processes, is probably the most mature photonics platform at present, and in many cases includes other materials such as silicon nitride for particular functions. Structured SOI is available from a variety of foundries and is an excellent choice for developing large-scale, multifunctional photonic chips. Significant progress has been made in components such as waveguides, resonators, modulators, photodetectors, multiplexers/demultiplexers, couplers/splitters, and optical switches (e.g. [1]).

Lasers suitable as on-chip sources have been developed and integrated by a variety of methods, which can be classified into 4 broad approaches: hybrid integration, wafer bonding, heterogenous epitaxial integration and silicon compatible lasers such as optically pumped Raman lasers [2] or GeSn alloy active region materials grown directly on silicon [3]. Hybrid integration involves the transfer of single amplifiers or laser chips onto the passive photonic integrated circuit and attaching via glue or solder in either a flip-chip, pick-and-place or transfer printing approach [4,5]. The latter uses an elastomer stamp, allowing for low-throughput, high-precision integration of fully processed III-V semiconductor devices onto Si substrates. By transferring a small area of the more costly III-V material, this technique is efficient in material usage. Furthermore, the process mitigates issues related to thermal expansion mismatch, as the small, thin structures are transferred at room temperature, although stress on the individual chips can still occur in the process. Some optical losses occur at the interface between active and passive materials, due to mismatch between the two waveguides and are further dependent on the quality of the alignment. The most commercially advanced heterogenous integration approach involves growing a III–V

#573505 https://doi.org/10.1364/OE.573505
Journal © 2025 Received 21 Jul 2025; revised 12 Nov 2025; accepted 12 Nov 2025; published 4 Dec 2025

Optics EXPRESS

epitaxial stack on a native substrate, followed by bonding the III–V wafer epitaxial side down onto a patterned SOI wafer [6,7] and is now demonstrated with Quantum dot (QD) material on 300 mm SOI [8]. The III-V device fabrication is then done post-bonding, which simplifies the alignment. However, this approach is quite inefficient in material usage and also suffers from the mismatch in size of typical silicon and III-V wafers. Stresses can build up during fabrication due to thermal expansion mismatch and typically, the light has to transfer between the active III-V and passive silicon sections though an interface between the materials or even a thin layer of glue and this can introduce some optical loss.

For the III-V active material, QDs offer excellent properties as a gain medium for stable on-chip laser operation, including low transparency current densities and low threshold when the loss is low [9], supporting energy-efficient operation. The broad spectral gain bandwidth at low current densities is also beneficial for high-temperature operation [10]. Additionally, QD lasers can have a low linewidth enhancement factor, and resilience to optical feedback [8,11,12]. However, QD materials have low maximum gain and thus this requires appropriate use in the PIC. QD lasers also tend to be much less sensitive to defects than quantum well materials [13] and this has resulted in the monolithic integration of III–V semiconductor materials on silicon (Si) substrates through heterogeneous epitaxial growth. QD III-V structures have been used for both long-lived O-band [14,15] and C-band [16] operation and considered for active-passive integration [17]. Here were focus on QD gain chips for hybrid integration or wafer bonding, which is closer to market than the more elegant epitaxial integration. Transfer-printed O-band InAs QD lasers have been demonstrated [5,18], however, the limited maximum gain amplitude of QD material poses challenges; at higher optical losses the lasing mechanism may switch from the ground state to the excited state, which is typically less efficient and is usually at an unsuitable wavelength for the application.

Optical loss is a critical factor in laser performance, as it directly impacts the threshold gain; the gain required for lasing. Higher optical losses increase the gain threshold, making it more challenging for the laser to achieve and sustain operation, particularly at the ground state where efficiency and performance are optimised.

For a laser fabricated from a hybrid integrated gain chip, where the laser mirrors are fabricated in silicon, the standard threshold gain equation for a Fabry-Perot cavity becomes (see Fig. 1):

$$G_{th} = \alpha_i + \frac{1}{2L} ln\left(\frac{1}{R_1 R_2}\right) + \frac{1}{L} ln\left(\frac{1}{T_1 T_2}\right) \tag{1}$$

where L is the length of III-V material producing gain in the composite cavity, α_i is the optical loss in the III-V material, R_1 and R_2 are the mirror reflectivity's of the cavity and T_1 and T_2 are the fractional transmission of light intensity at the interface between the III-V and the silicon waveguides in the forward and backward direction. We have assumed that the optical loss in the silicon waveguide is negligible. To compare laser cavities constructed entirely from III-V material with those constructed from a composite III-V and silicon waveguide structure we see that the composite cavity can have a lower threshold gain requirement if an improved mirror reflectivity in silicon can be obtained where the difference in loss with the III-V mirror reflectivity is greater than the loss introduced due to the transmission at the III-V to silicon interfaces. For O-band InAs QD waveguide material, the internal optical mode loss (α_i) typically ranges from 1 to 5 cm^{-1}. Figure 2 shows the calculated threshold gain requirement as a function of the transmission (coupling efficiency) between the III-V and silicon waveguide, where an α_i of 3 cm^{-1} is used. Three cases are shown with mirror reflectivity of 30%, 50% or 90% and the standard, all III-V cavity, G_{th}, assuming as-cleaved mirrors (R = 30%), is also indicated. Optimum performance of the laser will occur for the lowest value of threshold gain requirement and it is clear that high passive mirror reflectivity and high coupling efficiency are required to out-perform the standard III-V laser chip.

Optics EXPRESS

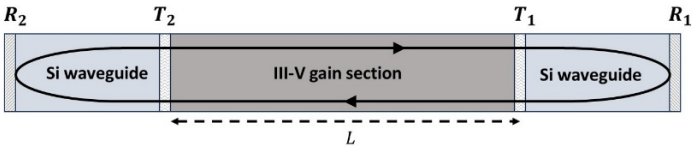

Fig. 1. schema of a hybrid integrated gain chip with the laser mirrors fabricated in the passive silicon material.

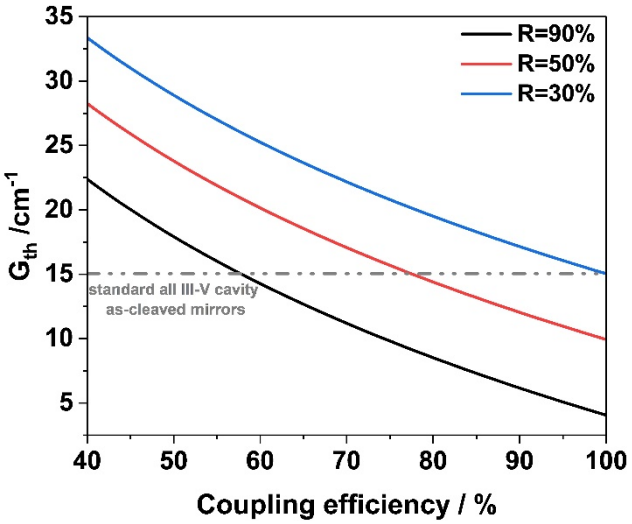

Fig. 2. Threshold gain requirement calculated using Eq. (1) for an active gain chip of length 1 mm, which is coupled at either end to a passive circuit providing 30%, 50% or 90% reflectors as a function of the coupling efficiency between III-V and the passive circuit. Dashed lines indicate the threshold gain requirement where the reflectors are integral to the III-V material.

For III-V gain chips transfer-printed onto Si, which require precise alignment for butt-coupled or for evanescently coupled waveguides, the coupling losses under good alignment can account for up to 30% of the optical power [5,18–20]. To address this, increasing the mirror reflectivity of both facets to around 90%, along with achieving a coupling efficiency in the range of 70 - 90%, is a widely used strategy. Higher passive mirror reflectivity helps compensate for the coupling losses to the Si waveguide, consequently reducing the gain threshold required for lasing.

As shown in Fig. 2, for a 1 mm active material length with mirrors having 90% reflectivity, the effect of coupling loss on the threshold gain requirement is significant and the impact of this is particularly important for QD gain materials where the maximum optical gain can be relatively low. While higher mirror reflectivity reduces the gain threshold, it introduces a trade-off by limiting the output power and slope efficiency, as less light exits the cavity. Hybrid integrated InAs/GaAs QD distributed Bragg reflector (DBR) lasers were previously demonstrated via transfer printing, where a 1.6 mm by 147 µm QD semiconductor optical amplifier (SOA) was printed over a Si waveguide [5]. Laser oscillation was achieved by combining the gain from the QD SOA with optical feedback provided by DBR mirrors with 90-86% reflectivity positioned at both ends of the silicon waveguide. This design achieved an output power of 7 mW at a drive current of 250 mA, with a slope efficiency of approximately 0.01 W/A [5]. Other reported demonstrations of InAs QD lasers on Si have achieved a slope efficiency in range of

Optics EXPRESS

0.04 W/A in [20]. This low slope efficiency may limit the functionality of these lasers in some PIC applications.

Improving the gain and reducing optical losses through improved QD design and growth remain key priorities and much effort has been extended in this direction. A further approach is optimising the transfer printed gain chip with the existing gain materials. In this paper the optimum design of the chip for transfer printing is discussed and measurements reported that illustrate the expected performance.

It is clear from Eq. (1) that if one of the laser mirrors is made within the III-V material we reduce the transmission loss by half. This also simplifies the alignment, including minimizing the gap or separation of the gain chip to the silicon waveguide, as this is only required on one side of the chip. This is the approach often used in flip chip mounting where a III-V chip with a high reflectivity dielectric mirror stack deposited on one facet is used. We assume that a single reflector in silicon is sufficient to create e.g. any required wavelength selectivity.

We now consider the options for implementing the reflector in the III-V material. A typical etched III-V mirror would yield a reflectivity of less than 30% or require high resolution lithography and high-quality etching to create a higher reflectivity grating structure. Here we suggest and test an alternative approach using multi-mode interference reflectors (MMIR)s which are simple to fabricate and yield reflectivity in the order of approximately 90%, thereby giving the advantage of a silicon reflector without the transmission loss. As described above we envisage that the output is taken from one side of the gain chip only simplifying the critical III-V waveguide to SOI waveguide alignment that would be required for full integration. Of course, one can also envisage the transfer of a working laser created entirely in III-V material, where the transmission loss at the III-V to SOI interface simply reduces the light level rather than affecting the threshold of the laser.

In the next sections we present three scenarios for gain chips and compare these options, in particular, we examine whether the threshold gain of Eq. (1) can be realised in typical QD materials. We also introduce the spatial mode selectivity that the MMIRs contribute and how we make use of this. We then evaluate the structures as standalone lasers, compared to that of simple Fabry-Perot ridge waveguide lasers (FP-RWG).

2. Device description

In what follows we briefly describe the design of the devices for use in three scenarios: a) a 1-port MMIR gain chip (Fig. 3(a)), (b) a 2-port MMIR gain chip (Fig. 3(b)) and (c) an on-chip MMIR laser constructed of a 1-port MMIR and 2-port MMIR (Fig. 3(c)).

The 1-port MMIR (type A, Fig. 3(a)) is designed such that, two angled reflectors are etched at a position to create an MMIR from a multi-mode interference structure (MMI) [21].

The 2-port MMIR structure (type B, Fig. 3(b)) uses the MMIR to fold the laser cavity back onto itself creating two outputs on the same side of the gain chip. This is useful for ease of alignment, however, it is initially unclear whether this design will operate as a single laser or as two coupled lasers (and this is further discussed in section 5). Clearly in the integrated format where further reflectors are placed in the silicon material it can facilitate, for example, coupled cavity type interaction to create supermodes with a larger free spectral range than a single cavity.

The structure illustrated in Fig. 3(c) (type C) is intended to be operated as a standalone laser. It integrates two MMIR mirrors with a single gain section and features an output port with 50% efficiency for the 1-port 2xMMIR configuration. The devices are designed with a multimode gain waveguide. An angled reflector is placed at either a single or dual imaging point to create high reflectivity of the mirrors at both ends of the laser. Coupling of the laser emission to a passive waveguide can be achieved using the unused second port of the 2-port MMIR. This also facilitates options such as the use of a tapered output to mode-match to the passive waveguide for better coupling.

Optics EXPRESS

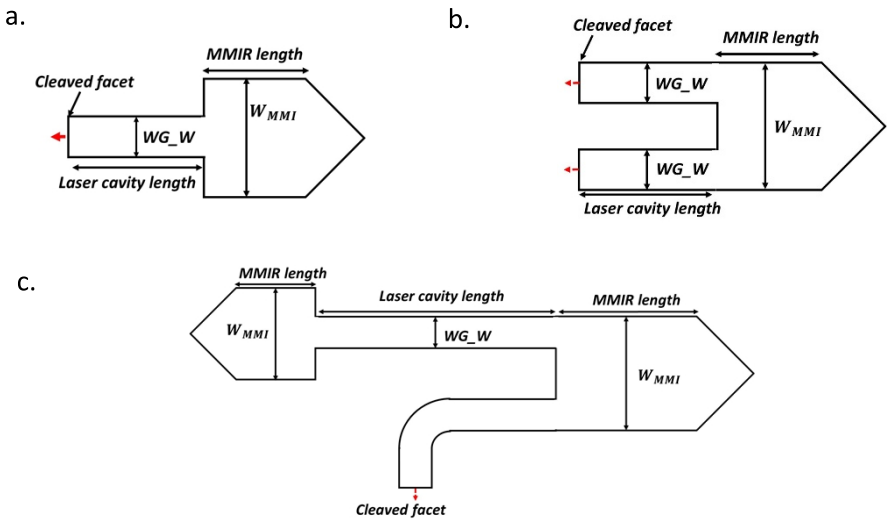

Fig. 3. Schema of the MMIR gain chips. a) 1-port MMIR gain chip b) 2-port MMIR gain chip and c) on-chip MMIR laser constructed from a) and b). When operated with a cleaved and uncoated output facet the resultant laser can be used to assess performance. When used as part of the PIC these would be directly coupled to the passive waveguide.

The three structures described are relatively simple to fabricate in the III-V material, with the reflectors etched in the same process step as the waveguide sections. The reduced number of fabrication steps, combined with high tolerances during fabrication to variation in the MMIR critical dimensions offers advantages over DBRs due to the ease of fabrication and MMIRs have already been applied in several circuits due to these advantages [22–25].

To examine the performance of structures of type A and B, cleaved facets are created on the opposite end of the cavity to the MMIRs. In practice in an integrated device the output would either be anti-reflection coated to allow butt coupling to an SOI structure, which would provide the second mirror and other functionality, or it would be evanescently coupled to the output waveguide. Using the as-cleaved III-V surface as the facet provides the minimum performance we would expect in the integrated device i.e., where an optimised integration technique would provide a reasonable coupling loss and a higher reflectivity mirror. For the type C structure, a cleaved facet on the output waveguide is made to monitor the light.

3. Simulation details and mode selectivity

The simulation method for the design of the MMIRs is discussed in detail in [26]. Here, we will introduce key features of the design without delving into the specifics of the simulation methods.

According to the self-imaging theory of MMIs, the MMIR length should be half of the original MMI's length and minimise the field intensity at the central tip of the mirror, where lithography limitations cause poor reflectivity.

Figure 4(a) shows the 1×2MMI that serves as the basis for creating the 1-port MMIR. The MMI width is set at a minimum of 6 µm to guide two image modes without encountering mirror corners. The input self-images occur at L = 91.5 µm, and to achieve the desired reflective power for the 1-port mirror, the MMIR is placed at L/2 = 45.75 µm, which is half of the MMI length (Fig. 4(b)). This ensures a 50:50% output, with two input images for the next calculation stage, and reduces the incident field at the mirror corner, thereby minimizing mirror loss.

Figure 5 displays the 2×2MMI used as the basis for constructing the 2-port MMIR, following the same principle. To fulfil the fabrication requirement, the MMI width is set at a minimum of

Optics EXPRESS

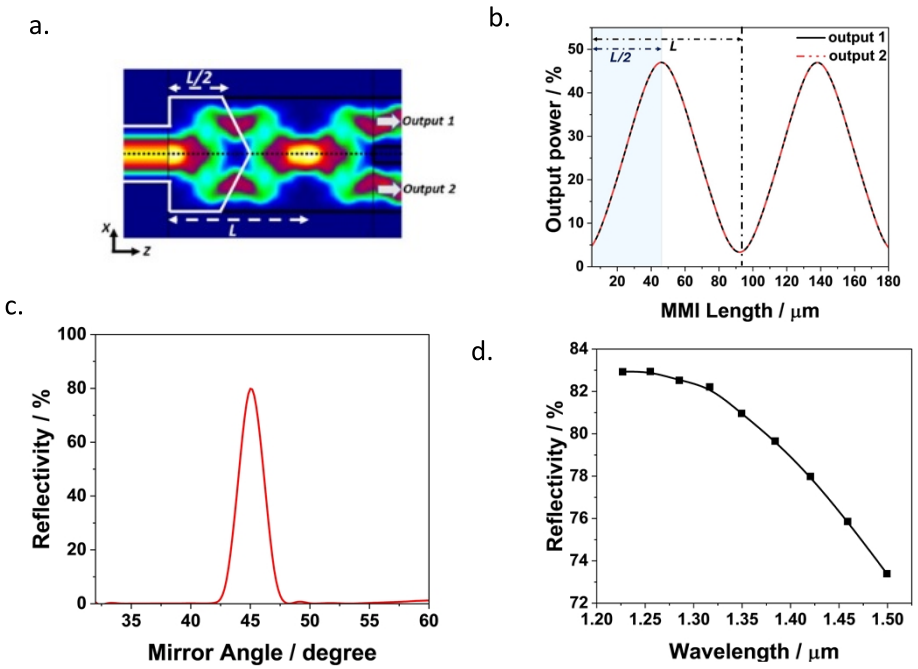

Fig. 4. a. Operation principle: field distribution simulation of 1×2 MMI (structure A) with the position of two superimposed angled facets marked. b. simulated 1×2MMI output power per MMI port as a function of MMI length. Note: data for positions marked as output 1 and output 2 overlay each other. c. 1-port MMIR reflectivity as a function of mirror angle at wavelength 1.31 μm. d. 1-port MMIR reflectivity of wavelength at mirror angle of 45°.

8 μm, ensuring an appropriate 2 μm gap between the two input/output waveguides with 3 μm width. The desired reflectivity of the designed 2-port MMIR in this work is 50:50% and maximum intensity occurs for an MMI of L = 331.25 μm (Fig. 5(b)).

To achieve this, the MMIR is placed at L/2 = 165.6 μm, which is half of the MMI length. The field distribution picture shows that the incident field at the mirror corner is minimized at this length, resulting in lower mirror loss.

The reflectivity of the fundamental TE_{00} mode is calculated from the overlap of the total power with the fundamental TE_{00} mode of the waveguide. Figures 4(c). and 5(c) show that both MMIRs exhibit a maximum reflectivity of about 85% at 45-degree mirror angles at a desired operating wavelength of 1.31 μm. Furthermore, Figs. 4(d) and 5(d) demonstrate that the reflectivity is achieved in a wide wavelength range of 1.2-1.35 μm. In the case of 2-port MMIR, the reflectivity per port is approximately 45%, resulting in a total reflectivity of 90%. Figure 5(d) illustrates that the condition for equal power reflectivity, for the two ports, at the designated wavelength does not apply at longer wavelengths. This behaviour is a result of the wavelength-dependent phase along the MMI waveguide, which alters the interference conditions between the supported modes. As the wavelength increases, the positions for constructive and destructive interference shift, thereby affecting the self-imaging characteristics of the device. Consequently, the optimal MMI length required for a 50:50 power split deviates from the initially designed value, resulting in asymmetric output power distributions and variations in reflectivity efficiency between the output ports (see Fig. 5(b) and (d)).

Structure C incorporates a 1×2 MMIR and a 2×2 MMIR, designed and optimized to combine reflected light from both mirror sides using a symmetric interference mechanism [27], These

Optics EXPRESS

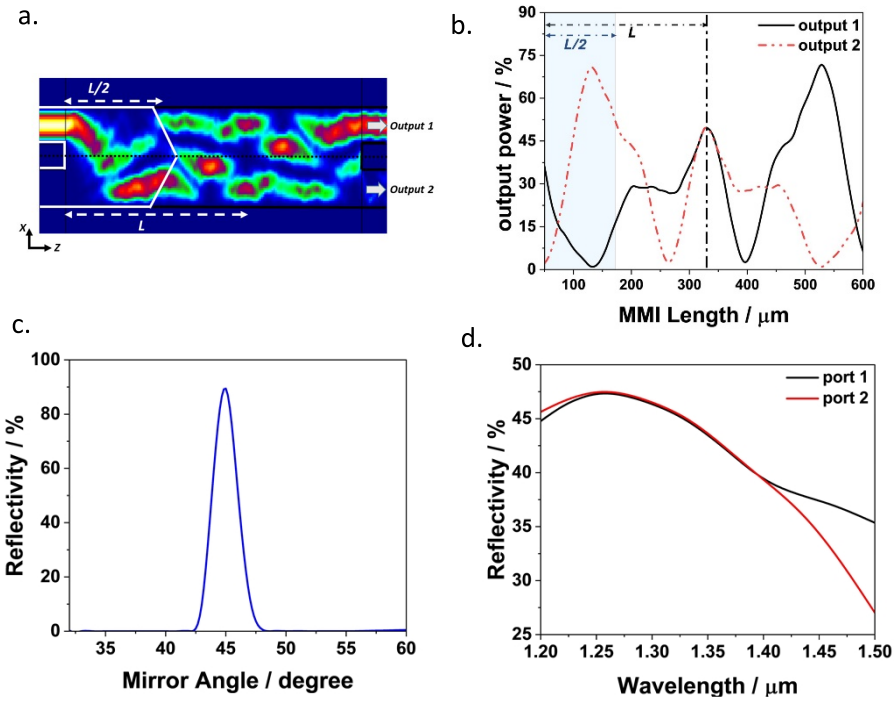

Fig. 5. a) Operation principle: field distributions simulation of 2×2 MMI (structure B) with the position of two superimposed angled facets marked, b) simulated 2×2MMI output power per MMI port as a function of MMI length. c) 2-port MMIR reflectivity as a function of mirror angle at 1.31 μm wavelength. d) 2-port MMIR reflectivity as function of wavelength at mirror angle 45°.

designs are intended explicitly for TE_{00}. Structure A is a 1-port MMIR laser that primarily supports the symmetric TE_{00} as detailed in [26].

Figure 6 illustrates the 2×2 MMI interference pattern resulting from the input field of the fundamental TE mode (TE_{00}) shown in Fig. 6(a), along with the first and second-order TE modes (TE_{01} and TE_{02}) displayed in Fig. 6(b) and 6(c). Figures 6(d) and 6(e) respectively show the power reflectance of the MMIR for these modes at output port-1 and port-2.

When a TE_{00} mode is fed into the input port of the 2×2 MMI coupler, its power is evenly distributed to the opposite output, resulting in constructive interference at the MMI coupler outputs, as demonstrated in the case shown in Fig. 6(a).

In Fig. 6(b), it is apparent that the TE_{01} modes with asymmetric order experience destructive interference at the centre, while TE_{02} modes with symmetric order have constructive interference, as seen in Fig. 6(c). When the input mode is TE_{00}, the MMI coupler combines the outgoing fields from MMIR with power-combining efficiencies of 48% for both output ports 1 and 2 for TE_{00} and around 2.3% for TE_{02}. For an incoming TE_{01} mode the reflection is about 40% and 43% for output port-1 and port-2, respectively. Additionally, for an incoming symmetric TE_{02}, the MMI coupler combines the outgoing field efficiencies of 20% for port-1 and 25% for port-2. It is important to note that the corner tip mirror used for the calculation is ideally perfect. However, due to lithography limitations, it will be slightly rounded in reality [22]. This means that incident TE_{01} and TE_{02} modes where there is field at the centre will not reflect properly, leading to even higher mode loss than predicted by the idealised calculation. Moreover, as seen in Fig. 6(b) and 6(c), these modes have substantial field distributed near the waveguide edges, making them

Optics EXPRESS

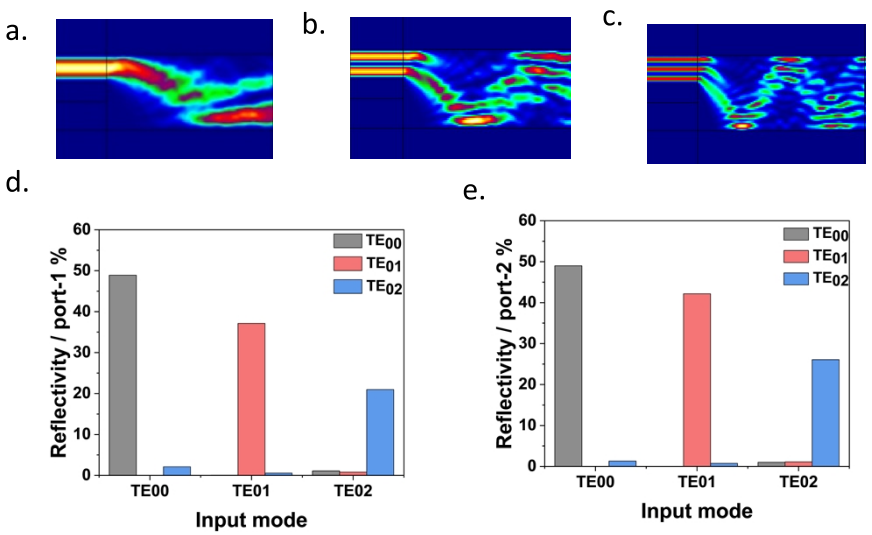

Fig. 6. Electric field intensity in the 2-port MMI coupler showing the wave propagation for: a. fundamental mode TE_{00}, b. second order straight mode TE_{01} as an example of asymmetric -order modes, and, c. third-order straight mode TE_{02} as an example of symmetric-order modes. d. and e. the MMIR power reflectivity for these different order input modes (marked on x-axis) into TE_{00} (gray), TE_{01} (red) and TE_{02} (blue), for port 1 and port 2 respectively.

more susceptible to scattering by sidewall roughness. This roughness on the sidewalls of an MMI structure has a negative impact on higher-order modes, leading to increased scattering, mode mismatch, and additional optical losses [28]. Consequently, the confinement decreases, mode conversion increases, and power transmission reduces for TE_{01} and TE_{02} modes within the MMIR [28,29].

In summary, structure A when operated as a 1-port MMIR laser primarily supports the symmetric TE_{00} mode. Structure B when operated as a 2-port MMIR laser supports both symmetric and asymmetric modes, but is expected to operate mainly for TE_{00}, due to the sidewall loss effect on higher order modes. Laser C combines both A and B, resulting in a combination that suppresses higher-order modes and amplifies the TE_{00} mode. The MMIR helps filter out asymmetric order modes from an input waveguide (see section 5 for further discussion), allowing what would otherwise be the single-mode ridge part of a laser to be slightly wider and thus more tolerant of fabrication uncertainty than a standalone Fabry-Perot ridge waveguide laser structure.

4. Device fabrication and characterization

To investigate device performance, QD MMIR RWG lasers were fabricated from a standard 1300 nm InGaAs-InAs QD laser stack grown by molecular beam epitaxy (MBE), which is represented in Fig. 7. Laser A features a 3 μm wide ridge combined with a 6 μm wide and 46 μm long MMIR section. Laser B has an 8 μm wide and 165 μm long MMIR section. Laser C integrates both MMIR mirrors with a cavity length of 1 mm. All MMIR lasers are designed with two 45-degree angled, deep-etched mirrors as termination points, as illustrated in Fig. 3. The MMIR and RWG were both defined using a single photolithography process. A Cl_2-based inductively coupled plasma (ICP) etch was used to transfer the pattern, with all devices etched down to the substrate. Dry-etch grade cyclotene (BCB) was utilised to planarise to the height of MMIR and RWG, followed by deposition of a Ti/Au p-contact. A back-side blanket-coat deposition of AuGe/Ni/Au provides a global n-contact metal following substrate thinning. All

Optics EXPRESS

samples were thinned to ~100 μm. An example of a fabricated device is shown in Fig. 8. The plan-view optical microscopy image illustrates three laser designs: Laser A, Laser B, and Laser C, shown in Fig. 8 (a), (b), and (c) respectively.

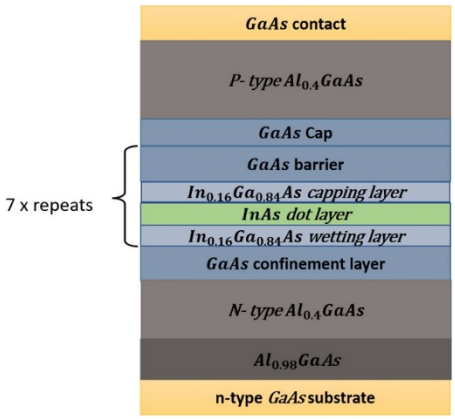

Fig. 7. Schema of InAs QD laser with 7 Dots-in-a-WELL (DWELL) layers.

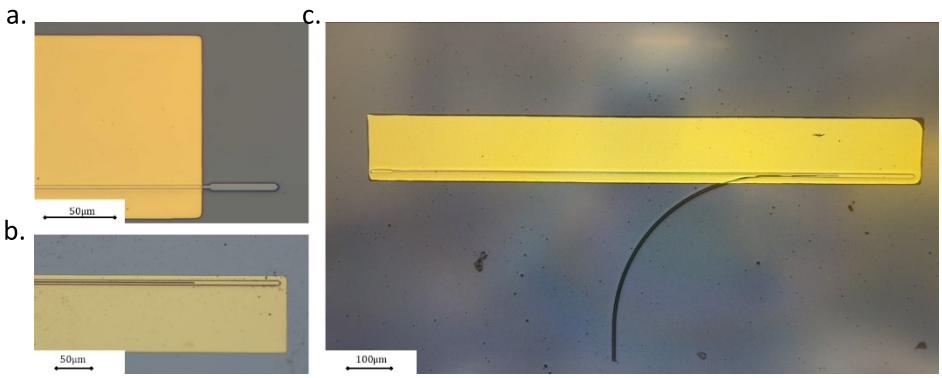

Fig. 8. Optical microscopic image of InAs QDs based MMIR laser for a. 1-port MMIR (Laser A). b. 2-port MMIR (Laser B) and c. on-chip MMIR laser (Laser C)

To assess the performance of MMIR lasers, each was characterised and compared with simple FP-RWG lasers. These FP-RWG lasers had two cleaved facets and were fabricated similarly, with a ridge width identical to that of the narrow ridge part of the MMIR lasers. The estimated cleaved facet reflectivity was calculated by applying the Fresnel equation for normal incidence and using the effective index of the mode. With the RWG width of 3 μm, the reflectivity was estimated to be 29%.

5. Experimental results

Figure 9 shows the power-current (P-I) characteristics for Laser A, Laser B, Laser C (illustrated in Fig. 3(a), 3(b) and 3(c) respectively), and two-cleaved-facet FP-RWG lasers. The cavity length for all MMIR lasers is 1 mm plus the MMIR lengths. The lasers were operated with a pulsed source with a 1000 ns pulse width at a 5 kHz repetition rate, resulting in a 0.5% duty cycle. The MMIR lasers demonstrated superior performance for all measured devices compared to the FP-RWG lasers in terms of threshold current and slope efficiency. For instance, the threshold

Optics EXPRESS

currents for Laser A, B, and C are 6, 14, and 11 mA, respectively, compared to 46 mA for the FP-RWG laser with a similar cavity length. Here for Laser B we consider the cavity length to be the length of a single arm waveguide port, as illustrated in Fig. 3(b). Later in this section we re-consider whether the relevant cavity length is that of the single arm or twice this. Since both arms of Laser B are identical, with the same length, and are pumped through a common metal this leads to a limited phase difference between them and as such it is unclear if lasers of type B should be treated as one cavity or two coupled cavities [30]. This will be further discussed by comparing the laser efficiency and the mode spacing later in the study.

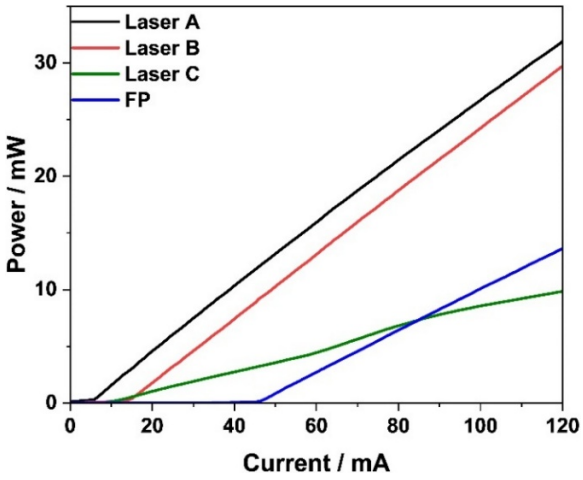

Fig. 9. Pulsed P-I curves for: 1-port MMIR laser (laser A), 2-port MMIR laser (Laser B), 1-port 2xMMIRs laser (laser C) and Fabry-Perot (FP-RWG) laser, of 1 mm cavity length at 25 °C.

The single facet slope efficiency, i.e. the slope of the P-I characteristics ($\Delta P/\Delta I$) in Fig. 9, is significantly higher for MMIR lasers than FP-RWG lasers. Laser A and B have a single facet slope efficiency of 0.26 W/A. However, laser C has a lower slope efficiency than the FP-RWG laser, which is 0.1 W/A compared to 0.15 W/A. Figure 10 displays the P-I characteristics for Laser A, B, and C, along with the FP-RWG laser, as a function of temperature, where the cavity length of all lasers is 1 mm + the relevant MMIR length. The graphs indicate that the threshold current of all MMIR lasers is less affected by temperature compared to the FP-RWG laser. Figure 10 c for Laser C shows a kink in the P–I curve, which is attributed to a switching between lasing modes. As will be explained later the longitudinal mode spacing observed for Laser C suggests a coupled cavity or vernier effect on the output spectrum. Figure 11 shows the threshold current density for various cavity lengths as a function of temperature. The MMIR lasers exhibit better performance for all lengths and temperatures, indicating the effectiveness of the reduced mirror loss.

Table 1 shows a comparison of single facet external quantum differential efficiency η^d_{ext} for these lasers with different cavity lengths based on the experimental results and compares these values with the calculated values based on the calculated mirror loss [29]. The efficiency of light emitted from the output facet η^d_{ext} can be calculated using the equation:

$$\eta^d_{ext} = \eta^d_{int} \frac{\alpha_{m-output}}{\alpha_i + \alpha_{m-total}} \tag{2}$$

η^d_{int} is the internal differential quantum efficiency which is 31%, derived from the $1/\eta^d_{ext}$ versus the cavity length [29]. $\alpha_{m-output}$ and $\alpha_{m-total}$ are the mirror loss for output facet and the total cavity, respectively, and α_i is the absorption loss which was determined to be around 1.6 cm^{-1}

Optics EXPRESS

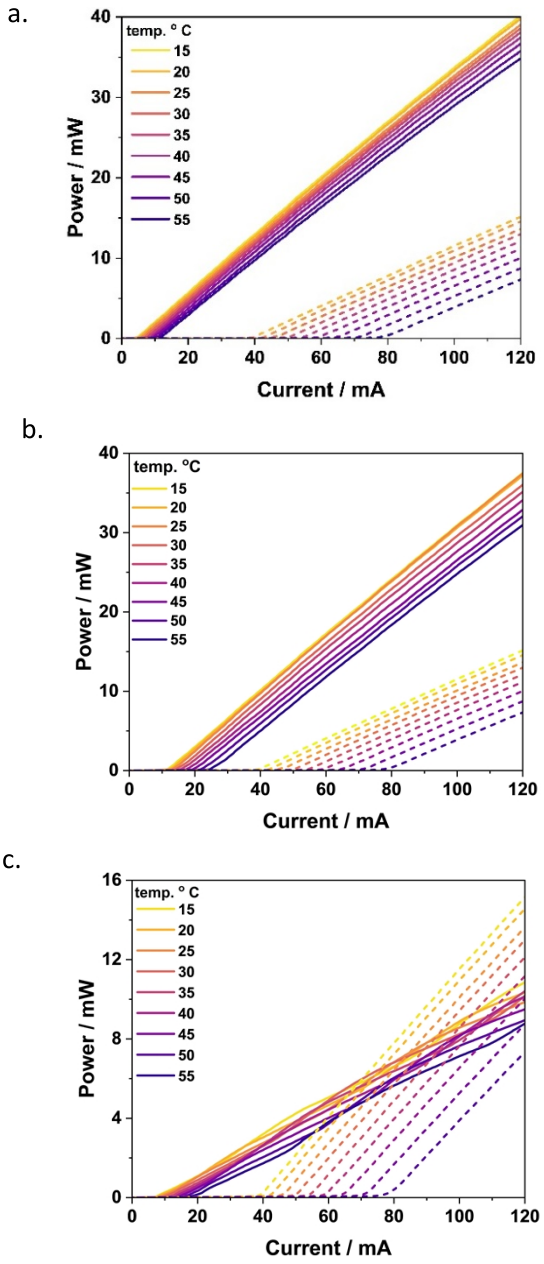

Fig. 10. Pulsed P-I curves for 1 mm length lasers as a function of temperature. a. 1-port MMIR laser (laser A), b. 2-port MMIR laser (Laser B), c.1-port 2xMMIRs laser (laser C) (solid line) compared to FP-RWG (dots line).

for this InAs QD structure using the segmented contact method [29]. The table shows that the experimentally derived η_{ext}^{d} values and those calculated based on mirror loss are consistent across all laser devices and cavity lengths. This demonstrates that the modelled reflectivities can be achieved in the experimental MMIRs.

From Table 1, the slope efficiency of Laser A is approximately equivalent to the two-facet slope efficiency of the FP-RWG laser; this indicates the high MMIR reflectivity. The slope efficiency

Optics EXPRESS

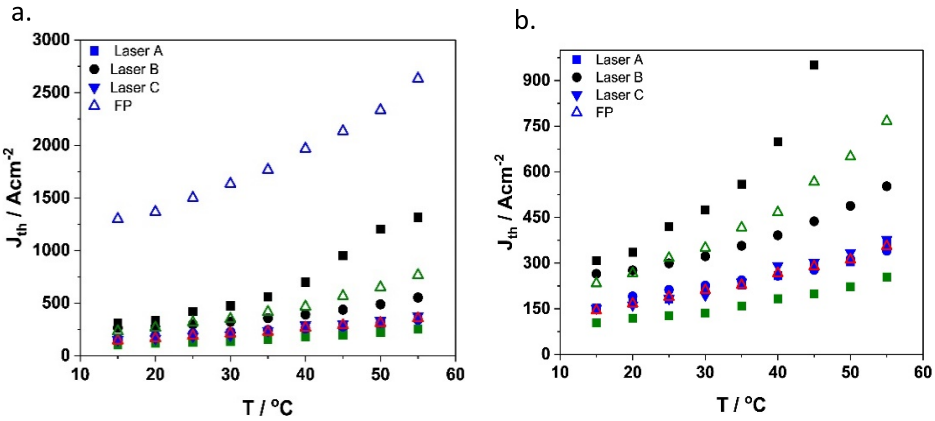

Fig. 11. a. Threshold current density for MMIR (solid symbols) and FP-RWG (open symbols) lasers for different cavity length as function of temperature. black: 0.5 mm, blue: 1 mm, green: 2 mm and red: 3-mm cavity length. b. zoom in on comparison of different MMIR lasers. (note that Laser B cavity length, means the length per single waveguides arm).

Table 1. Single-facet external differential efficiency for FP-RWG and MMIR lasers derived from experiment (column4) and as calculated (column 5). Where ΔP/ΔI is the slope of P-I above threshold, q is the electronic charge, h is Planck's constant, and c is the speed of light. $\alpha_{m-output}$, and $\alpha_{m-total}$ are the mirror losses for output mirror and both mirrors respectively, α_i is the optical mode loss.

Laser type	Cavity length /mm	$\frac{\Delta P}{\Delta I}$ W/A	$\eta_{ext}^{d} = \frac{\Delta P}{\Delta I} \times \frac{q\lambda}{hc}$	$\eta_{ext}^{d} = \eta_{int}^{d} \frac{\alpha_{m-output}}{\alpha_i + \alpha_{m-total}}$
FP-RWG	1	0.15	0.146	0.147
Laser A	0.5458	0.275	0.287	0.287
	1.0458	0.256	0.27	0.27
Laser B	0.666	0.275	0.287	0.287
	1.166	0.26	0.27	0.27
Laser C	1.2	0.1	0.11	0.246

for Laser B with cavity lengths of 0.666 and 1.166 mm is similar to Laser A's single-facet slope efficiency with a similar cavity length (see Fig. 3) but this is expected whether Laser B operates as two separate laser cavities or a single cavity. The wavelength and mode spacing data presented later does differentiate between these two possibilities.

Laser C shows the lowest external efficiency, as Laser C includes a high reflectivity mirror, with more than 90% reflectivity on the left-hand side at the 1-port MMIR, and a 2-port MMIR on the right-hand facet, with a one port reflectivity of 50%. The higher mirror reflectivity reduces the threshold current; However, the external laser efficiency is affected by the higher reflectivity mirror, causing a lower slope efficiency compared to other laser devices. In addition, for ease of fabrication the emitted light travels through an unpumped section of III-V material including a curved waveguide before encountering a further III-V – air interface. The absorption loss of the unpumped waveguide, the extra interface and radiative loss due to the curved waveguide, will contribute further to a decrease in the measured output power.

The lasing wavelength as a function of temperature is plotted for the different lasers in Fig. 12. The wavelength spectrum is measured using a Yokogawa spectrum analyser with light collected from the device facet with an optical fiber. The result in Fig. 12 demonstrates that the MMIR lasers function on the ground state up to at least 55°C, whereas the FP-RWG lasers operate on the excited state for the shorter cavity lengths. Whilst the MMIR lasers do have a slightly longer gain length, due to the added length of the MMIR section itself (45.75 μm for type A, 165.5 μm for

Optics EXPRESS

type B and 211.3 µm for type C) this does not explain the differences in lasing wavelength. Even the 2 mm long FP-RWG laser only operates on the ground state up to 45 °C. Laser A, with a cavity length of 0.5 mm, exhibits a mode-hopping effect at high temperatures (50-55°C), as the current density increases. These conditions cause both the longitudinal mode wavelengths and the gain peak wavelength to shift toward longer wavelengths, but at different rates. Because the gain peak shifts more rapidly than the cavity modes, it successively aligns with different longitudinal modes, resulting in abrupt transitions in the lasing wavelength, characteristic of mode hopping [31]. These results are consistent with the MMIR lasers having reduced gain requirement allowing ground state lasing even at elevated temperatures, where the thermal distribution of charge carriers reduces the gain magnitude for a given carrier density [31].

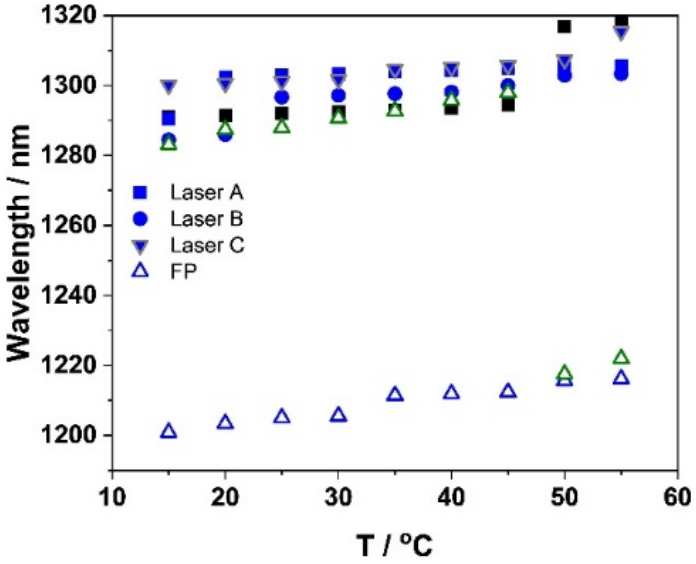

Fig. 12. Peak lasing wavelength as function of temperature for MMIR laser of type A, B, and C, and FP-RWG laser. Black:0.5 mm, blue: 1 mm, and green: 2 mm cavity length.

The detailed spectra of the MMIR lasers of type A, B and C operating at 25 °C are plotted in Fig. 13 and the FP-RWG spectra are shown in Fig. 14. The FP-RWG spectra with cavity lengths of 1 mm, 2 mm, and 3 mm exhibit multiple lateral and longitudinal modes for all cavity lengths due to the 3 µm ridge width. Whereas the MMIR laser spectra of Fig. 13 do not have any obvious high order lateral modes, supporting the idea that the MMIR acts as a mode filter.

The lasers of type A have total cavity lengths of 546 µm and 1046 µm (including the MMIR section) and the lasers of type B have cavity lengths of 666 µm and 1166 µm, whereas lasers of type C are 1211 µm. These lasers have modes covering a smaller spectral wavelength range than the FP-RWG lasers. The reduced spectral range or width of the MMIR lasers is indicative of a lower mirror loss, which leads to a lower gain requirement, less broad gain spectrum and a lower threshold carrier density [31]. Table 2 compares the mode spacing between Laser A and B taken from the experimental results presented in Fig. 13(a) and 12(b). The mode spacing was calculated using Fimmwave software [32] based on the equation:

$$\Delta\lambda = \frac{\lambda^2}{2\left(\left(n_{eff} + \lambda\frac{dn}{d\lambda}\right)_{laser\ cavity} L_{laser\ cavity} + \left(n_{eff} + \lambda\frac{dn}{d\lambda}\right)_{MMIR} L_{MMIR}\right)} \tag{3}$$

For Laser B the length used is the length per single waveguide arm and the table shows good agreement between the calculated mode spacing, using Eq. (3) based on Fimmwave software

Optics EXPRESS

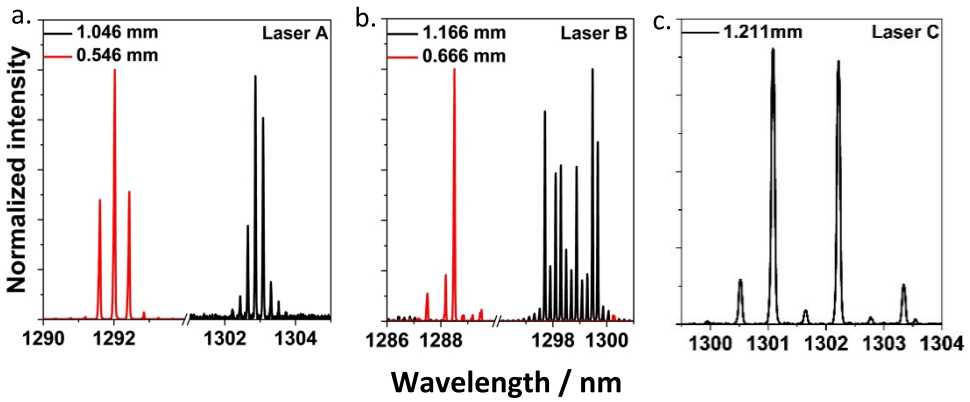

Fig. 13. Emission spectra for MMIR lasers a. type A, with 0.546- and 1.046-mm cavity length b. type B with cavity length 0.666- and 1.166-mm c. type C with 1.211 mm cavity length at 25 ^{o}C

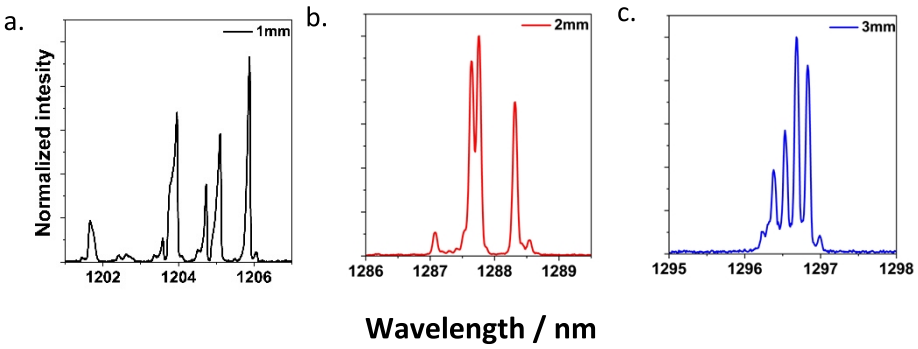

Fig. 14. Emission spectra for FP-RWG lasers for a. 1 mm, b. 2 mm, c. 3 mm cavity length, respectively, at 25 ^{o}C.

simulation result when the individual arm length is used as the laser cavity length, and the experimental result in Fig. 12. This result indicates that Laser B works as two separate laser cavities with the same cavity length and mirror reflectivity (see Fig. 3). Both are pumped through a common metal contact, which results in limited phase difference between them. Consequently, both waveguides provide additional feedback to each other via the MMIR with the same phase, which supports single arm operation over a single cavity of double the length [29,33]. This makes two lasers that are highly efficient.

For lasers of type C the mode spacing is much larger and characteristic of the behaviour of two coupled cavities where a supermode is created as two modes from the different cavities overlap. We believe this may originate due to feedback from the output facet of the waveguide which is external to the laser, and which was left as-cleaved. This has well known but important implications if the laser is used in a PIC, where methods to reduce back reflections, such as an anti-reflection coating should be used.

6. Summarising performance

The results indicate the advantages of having one high reflectivity mirror on-chip as compared to two 30% reflectors and, by consideration of Eq. (1), to having two interfaces and high reflectivity external mirrors. To emphasise and characterise this more completely we have used the segmented

Optics EXPRESS

contact technique [34] to measure the peak modal gain available from the quantum dot waveguide material. Results from this study are plotted in Fig. 15 alongside the values of calculated mirror loss and measured threshold current density for MMIR lasers of type A, B and C. Results indicate that, except for the 546 µm long laser of type A, the MMIR lasers are all operating in a region of the gain-current density characteristic where gain saturation is minimal.

Table 2. The experimental mode spacing $\Delta\lambda_{experimental}$ obtained from Fig 11 and the theoretical mode spacing $\Delta\lambda_{theoretical}$ calculated using Fimmwave software based on Eq. (3) for Lasers of type A and B.

Laser type	Cavity length /mm	$\Delta\ \lambda_{theoretical}$/ nm	$\Delta\ \lambda_{experimental}$ / nm
Laser A	0.5458	0.43	0.42
	1.0458	0.23	0.22
	2.0458	0.12	0.11
Laser B	0.666	0.34	0.34
	1.166	0.196	0.196
	2.166	0.11	0.1
Laser C	1.2		1.34

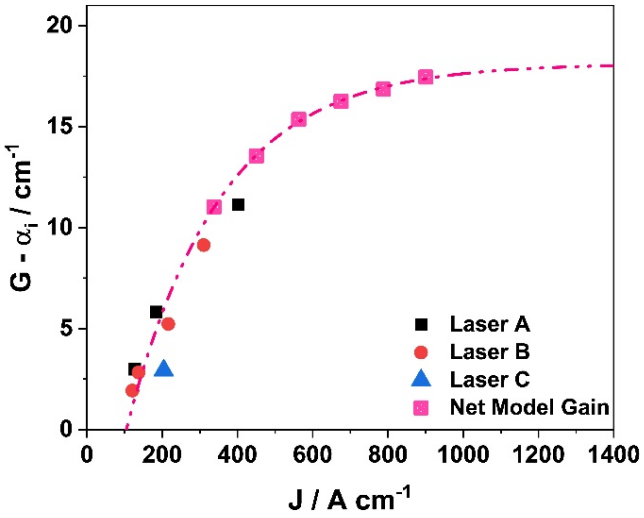

Fig. 15. Peak Net Modal gain measurement from the segmented contact technique implemented as in [34] plotted as mirror loss and compared to the calculated mirror loss and threshold current density of MMIR lasers of type A, B and C and of different cavity lengths and at 21 °C.

The higher reflectivity mirror of the MMIR results in lasers with a lower threshold current, which is also less affected by temperature than FP-RWG lasers of the same length. This is due to the saturated nature of the QD gain-current density curve as seen in Fig. 15 [35]. In addition in the MMIR lasers, due to the mode filtering as observed in the laser spectra, the higher order lateral modes are not as amplified as the ground state mode and therefore current density used for these amplification processes in the FP laser is saved in the MMIR laser.

The high MMIR reflectivity reduces the threshold gain requirement while the output power and slope efficiency depends on the output coupler or the interface to the silicon photonics circuit. This can be optimised using Fig. 15 to estimate the optimum coupling loss that can be incurred.

Optics EXPRESS

7. Summary

We have examined options for integrating III-V gain materials with SOI or other passive photonic circuits. We have demonstrated that an MMIR combined with a III-V gain region can produce low threshold, and low temperature dependence of threshold current lasers which operate in the O-band with single spatial mode and with relatively high efficiency. By consideration of composite cavity lasers it is clear that such structures offer advantages for hybrid integration. These structures are relatively easy to fabricate and have a small footprint and can be placed and oriented anywhere in the circuit. The MMIR lasers also have a high optical slope efficiency, indicating a mirror reflectivity of the non-output mirror of above 90%.

We introduce one and two port structures, where the outputs are on the same side of the gain chip for ease of integration. Relatively high ouptut power demonstrates the suitability of MMIR gain chips as on-chip elements for integrated photonics. Measured gain data can be used to predict suitable coupling loss targets for high performance operation.

Funding. Engineering and Physical Sciences Research Council (EP/Z532848/1, EP/T028475/1).

Acknowledgment. Devices were fabricated in the Institute for Compound Semiconductor cleanroom, at Cardiff University. This work was supported by the EPSRC funded Compound Semiconductor Manufacturing Hub for a Sustainable Future (Grant No. EP/Z532848/1) and the EPSRC QUDOS Programme (Grant No. EP/T028475/1).

Disclosures. The authors declare no conflicts of interest.

Data availability. Data underlying the results presented in this paper are available in Ref. [36].

References

1. L. Chrostowski and M. E. Hochberg, *Silicon photonics design* (Cambridge University Press, 2015).
2. H. Rong, S. Xu, Y.-H. Kuo, *et al.*, "Low-threshold continuous-wave Raman silicon laser," Nat. Photonics **1**(4), 232–237 (2007).
3. S. Acharya, H. Stanchu, R. Kumar, *et al.*, "Electrically Injected Mid-Infrared GeSn Laser on Si Operating at 140 K," IEEE J. Sel. Top. Quantum Electron. **31**(1: SiGeSn Infrared Photon), 1–7 (2025).
4. A. Moscoso-Martir, F. Merget, J. Mueller, *et al.*, *Hybrid silicon photonics flip-chip laser integration with vertical self-alignment*, (IEEE), pp. 1–4.
5. N. Morais, J. Fujikata, J. Kwoen, *et al.*, "Hybrid distributed Bragg reflector laser on Si with a transfer printed InAs/GaAs quantum dot amplifier," Opt. Express **32**(3), 4295–4304 (2024).
6. R. Jones, P. Doussiere, J. B. Driscoll, *et al.*, "Heterogeneously Integrated InP\/Silicon Photonics: Fabricating Fully Functional Transceivers," IEEE Nanotechnology Mag. **13**(2), 17–26 (2019).
7. C. Yang, L. Liang, L. Qin, *et al.*, "Advances in silicon-based, integrated tunable semiconductor lasers," Nanophotonics **12**(2), 197–217 (2023).
8. D. Huang, X. Wu, S. Yerkes, *et al.*, "Feedback tolerant quantum dot lasers integrated with 300 mm silicon photonics," J. Lightwave Technol. **43**(4), 1–6 (2024).
9. D. G. Deppe, K. Shavritranuruk, G. Ozgur, *et al.*, "Quantum dot laser diode with low threshold and low internal loss," Electron. Lett. **45**(1), 54–56 (2009).
10. P. Mishra, L. Jarvis, C. Hodges, *et al.*, "High Temperature Operation of Co-doped InAs Quantum Dot Laser for O-Band Emission," IEEE Photonics J. **17**(3), 1–6 (2025).
11. D. O'Brien, S. P. Hegarty, G. Huyet, *et al.*, "Feedback sensitivity of 1.3 µm InAs/GaAs quantum dot lasers," Electron. Lett. **39**(25), 1819–1820 (2003).
12. H. Huang, J. Duan, D. Jung, *et al.*, "Analysis of the optical feedback dynamics in InAs/GaAs quantum dot lasers directly grown on silicon," J. Opt. Soc. Am. B **35**(11), 2780–2787 (2018).
13. D. Jung, R. Herrick, J. Norman, *et al.*, "Impact of threading dislocation density on the lifetime of InAs quantum dot lasers on Si," Appl. Phys. Lett. **112**(15), 153507 (2018).
14. S. Chen, W. Li, J. Wu, *et al.*, "Electrically pumped continuous-wave III-V quantum dot lasers on silicon," Nat. Photonics **10**(5), 307–311 (2016).
15. C. Shang, E. Hughes, Y. Wan, *et al.*, "High-temperature reliable quantum-dot lasers on Si with misfit and threading dislocation filters," Optica **8**(5), 749 (2021).
16. Y. Han, Z. Yan, W. K. Ng, *et al.*, "Bufferless 1.5 µm III-V lasers grown on Si-photonics 220 nm silicon-on-insulator platforms," Optica **7**(2), 148–153 (2020).
17. Z. Zhang, C. Shang, J. C. Norman, *et al.*, "Monolithic Passive− Active Integration of Epitaxially Grown Quantum Dot Lasers on Silicon," physica status solidi (a) **219**(4), 2100522 (2022).
18. A. Uzun, F. B. Atar, S. Iadanza, *et al.*, "Integration of Edge-Emitting Quantum Dot Lasers with Different Waveguide Platforms using Micro-Transfer Printing," IEEE J. Sel. Top. Quantum Electron. **29**, 1–11 (2023).

Optics EXPRESS

19. B. Jang, K. Tanabe, S. Kako, *et al.*, "A hybrid silicon evanescent quantum dot laser," Appl. Phys. Express **9**(9), 92102 (2016).
20. Y. Wan, C. Xiang, J. Guo, *et al.*, "High speed evanescent quantum-dot lasers on Si," Laser Photonics Rev. **15**(8), 2100057 (2021).
21. L. B. Soldano and E. C. M. Pennings, "Optical multi-mode interference devices based on self-imaging: principles and applications," J. Lightwave Technol. **13**(4), 615–627 (1995).
22. Z. Jing, E. Kleijn, M. K. Smit, *et al.*, *Novel lasers using multimode interference reflector*, (IEEE), pp. 1–2.
23. J. Zhao, E. Kleijn, P. J. Williams, *et al.*, *On-chip laser with multimode interference reflectors realized in a generic integration platform*, (IEEE), pp. 1–4.
24. C. Gordón, R. Guzmán, V. Corral, *et al.*, "On-Chip Colliding Pulse Mode-locked laser diode (OCCP-MLLD) using multimode interference reflectors," Opt. Express **23**(11), 14666–14676 (2015).
25. F. T. Albeladi, C. P. Allford, S.-J. Gillgrass, *et al.*, *Multi-mode interference reflector InAs-QD mode-locked laser for integrated photonics*, (IEEE), pp. 1–2.
26. F. Albeladi, S.-J. Gillgrass, J. Nabialek, *et al.*, "Design and Characterisation of Multi-Mode Interference Reflector Lasers for Integrated Photonics," J. Phys. D: Appl. Phys. **56**(38), 384001 (2023).
27. J. Leuthold, R. Hess, J. Eckner, *et al.*, "Spatial mode filters realized with multimode interference couplers," Opt. Lett. **21**(11), 836–838 (1996).
28. A. Yakuhina, A. Kadochkin, V. Svetukhin, *et al.*, "Investigation of Side Wall Roughness Effect on Optical Losses in a Multimode Si3N4 Waveguide Formed on a Quartz Substrate," Photonics **7**(4), 104 (2020).
29. F. Albeladi, "Advancing integrated photonic circuits: Design, fabrication, and characterization of key photonic components," (2024).
30. D. d'Agostino, D. Lenstra, H. Ambrosius, *et al.*, "Coupled cavity laser based on anti-resonant imaging via multimode interference," Opt. Lett. **40**(4), 653–656 (2015).
31. P. M. Smowton, I. C. Sandall, D. J. Mowbray, *et al.*, "Temperature-Dependent Gain and Threshold in P-Doped Quantum Dot Lasers," IEEE J. Sel. Top. Quantum Electron. **13**(5), 1261–1266 (2007).
32. P. D. Ltd, "FIMMWAVE," https://www.photond.com/products/fimmwave.htm.
33. D. D'Agostino, D. Lenstra, H. Ambrosius, *et al.*, "A coupled cavity laser based on a multimode interference reflector," pp. Tu-3a.
34. P. Blood, G. M. Lewis, P. M. Smowton, *et al.*, "Characterization of semiconductor laser gain media by the segmented contact method," IEEE J. Sel. Top. Quantum Electron. **9**(5), 1275–1282 (2003).
35. P. M. Smowton, I. C. Sandall, H. Y. Liu, *et al.*, "Gain in p -doped quantum dot lasers," J. Appl. Phys. **101**(1), 013107 (2007).
36. https://doi.org/10.17035/cardiff.29591231.